Journal of Materials Chemistry C

ROYAL SOCIETY OF CHEMISTRY

PAPER

View Article Online
View Journal

Cite this: DOI: 10.1039/d5tc03933a

Ion transport in triphenylene metal–organic columnar mesophases

Rubén Chico, [a] María Jesús Baena, [a] Cristián Cuerva, *[b] Rainer Schmidt, [c] Bertrand Donnio *[d] and Silverio Coco *[a]

Received 4th November 2025,
Accepted 14th December 2025

DOI: 10.1039/d5tc03933a

rsc.li/materials-c

Ionic liquid crystals (iLCs) constitute an emerging materials type that combines the properties of an ionic liquid, such as ionic mobility, with the supramolecular organization of a liquid crystal. This makes them suitable candidates for applications such as anisotropic ion conductors and next-generation energy storage systems. In this work, we report ion conducting columnar mesophases based on bis(triphenylene-isocyanide) metal complexes of the type $[M(CNR)_2]Y$ (CNR = 2-(6-(4-isocyanophenoxy)hexyloxy)-3,6,7,10,11-pentakisdodecyloxy-triphenylene; M = Ag(I), Au(I); Y = NO_3^-, BF_4^-). All the gold and silver complexes display enantiotropic mesomorphism in the temperature range 35–80 °C. They self-assemble into rectangular columnar mesophases, whose X-ray diffraction profiles reveal the simultaneous stacking of triphenylene disks into one-dimensional columns and the aggregation of metallic fragments assembled into filaments that are arranged parallel between the triphenylene columns. The ionic conductivity of these mesophases is based on the counterion mobility and increases regularly as the molecular slice thickness increases along the columns, ranging from 1.70×10^{-9} to 1.64×10^{-8} S cm^{-1}. Although the conductivity values obtained so far are lower than those required for commercial displays, our results demonstrate the key role of packing efficiency in ion transport in soft materials, and the potential of organic/inorganic nanosegregated mesophases to develop tailored and advanced ion-conducting materials. The gold and silver complexes display fluorescence behavior related to the triphenylene core in solution.

Introduction

Ionic liquid crystals (iLCs) constitute a well-defined type of self-organized soft systems, which combine the characteristic properties of an ionic liquid, such as high ionic mobility, with the supramolecular organization and fluidity of the mesophase of a liquid crystal.[1–8] Many studies show that these materials display unique properties, making them suitable candidates for a number of potential applications, particularly for sustainable energy-related devices, such as fuel cells, batteries and supercapacitors.[1,9] Ionic liquid crystals have also generated great interest as ordered reaction media,[10] anisotropic ionic conductors,[11,12] and even in biology as siRNA transfection vectors.[13] The vast majority of reports on iLCs deals with systems that bear one or two alkyl substituents connected to either a small ionic moiety or a rod-like core, showing mainly smectic phases.[1,14–16] In contrast, only a few studies on ionic liquid crystals with a discotic core that display columnar mesomorphism have been reported.[5,6,17–21] A significant number of them are based on substituted triphenylenes. Such triphenylene-based discotic mesogens constitute a classical example of self-organized columnar materials, whose properties can be modulated through chemical functionalization of the triphenylene unit with different groups.[22–25] This strategy is apparently simple but usually involves complicated synthesis and complex purification procedures. Some ammonium, guanidinium, imidazolium, and pyridinium triphenylene salts displaying ionic columnar mesophases have been prepared. Other examples include crown ether triphenylene derivatives,[26–30] where the coordination of alkaline cations to the crown ether group produces mesophase stabilization.

Many applications of iLCs require materials with high ionic conductivities. In this regard, it is well known that significantly enhanced ionic conductivity is achieved in columnar mesophases containing nanosegregated ionic domains, due to the increased mobility of the ionic moieties.[5,31]

On the other hand, a simple, versatile and well-known way to tune the thermal, optical and electronic properties of neutral

[a] IU CINQUIMA/Química Inorgánica, Facultad de Ciencias, Universidad de Valladolid, 47011, Valladolid, Castilla y León, Spain. E-mail: silverio.coco@uva.es
[b] MatMoPol, Departamento de Química Inorgánica, Facultad de Ciencias Químicas, Universidad Complutense de Madrid, Ciudad Universitaria, E-28040, Madrid, Spain. E-mail: c.cuerva@ucm.es
[c] GFMC, Departamento de Física de Materiales, Universidad Complutense de Madrid, Ciudad Universitaria, E-28040, Madrid, Spain
[d] Institut de Physique et Chimie des Matériaux de Strasbourg (IPCMS), CNRS-Université de Strasbourg (UMR 7504), 67034, Strasbourg, France. E-mail: bertrand.donnio@ipcms.unistra.fr

triphenylene liquid crystals involves the use of transition metals as linking groups, by coordination of functionalized triphenylene fragments that can act as ligands.[32–39] With this strategy, we have previously reported on semiconducting and luminescent mesophases based on mesomorphic organometallic complexes containing triphenylene moieties,[40–46] where π-stacking of the triphenylene discs in columns and aggregation of the metallic moieties into segregated columnar zones coexist in a well ordered manner in the mesophase. Now, we have investigated the use of cationic metal synthons as linking groups in functionalized triphenylene with the aim of obtaining organometallic triphenylene columnar mesophases prone to display ion transport. In this work, we report uncommon ionic conducting columnar mesophases based on mesomorphic bis(triphenylene-isocyanide) metal complexes of the type $[M(CNR)_2]Y$ (CNR = 2-(6-(4-isocyanophenoxy)hexyloxy)-3,6,7,10,11-pentakisdodecyloxy-triphenylene; M = Ag(I), Au(I); Y = NO_3^-, BF_4^-), *i.e.* $[Ag(CNR)_2]NO_3$ (compound **1**), $[Ag(CNR)_2]BF_4$ (compound **2**), $[Au(CNR)_2]NO_3$ (compound **3**), and $[Au(CNR)_2]BF_4$ (compound **4**). The effect of the metal cation and the anion on the ionic conductivity of the system is discussed.

Results and discussion

Synthesis

The isocyanide metal complexes were prepared by reaction of two equivalents of 2-(6-(4-isocyanophenoxy)hexyloxy)-3,6,7,10,11-pentakisdodecyloxy-triphenylene (CNR)[41] with the corresponding metal precursors, as shown in Scheme 1. All the complexes prepared were isolated as yellow waxy solids in high yield. Full synthetic description, C, H, and N microanalyses, MALDI-TOF mass spectra, and relevant IR and NMR characterization data are given in the SI.

The UV-Vis absorption and fluorescence spectra of the metal complexes in dichloromethane solution are all very similar (Fig. 1 and 2, and Table 1), displaying spectral patterns typical of triphenylene chromophores, and analogous to that of the free isocyanide ligand and related neutral isocyanide complexes.[42]

As observed in the free ligand, the luminescence is lost in the solid state (room temperature and 77 K) and in the mesophase.

Thermal behavior and self-organization properties

The mesomorphic behavior of the metal isocyanide complexes **1–4** has been studied using polarized optical microscopy (POM), differential scanning calorimetry (DSC) and X-ray

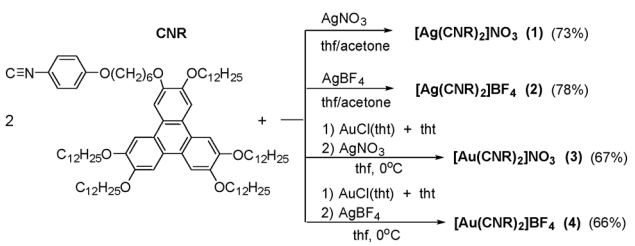

Scheme 1 Synthesis of the silver and gold complexes.

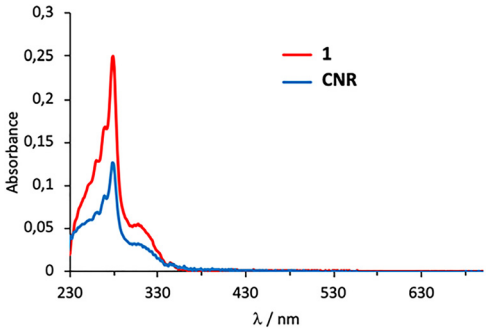

Fig. 1 UV-Visible spectra of the free isocyanide ligand (**CNR**) and **1** in dichloromethane (10^{-6} M) at 298 K.

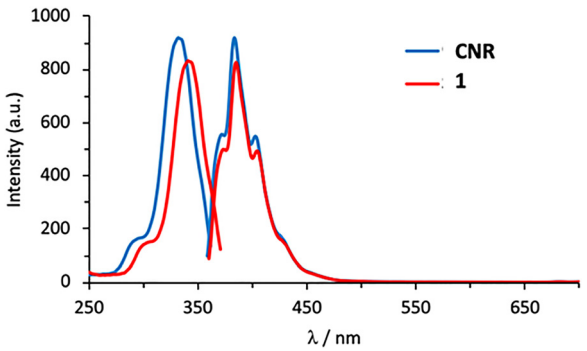

Fig. 2 Excitation (left) and emission (right) spectra of the free isocyanide ligand (**CNR**) and **1** in dichloromethane (10^{-6} M) at 298 K.

scattering measurements. Transition temperatures and thermal data are gathered in Table 2.

Regarding the thermal stability of the compounds studied, thermogravimetric analysis shows good thermal stability, even in the isotropic liquid (Fig. S28–S31). This contrasts with the poor thermal stability of related cationic nitrate gold complexes without triphenylene substituents,[47] where the thermal instability is associated with the easy decomposition of the anion in the presence of gold cations.[48] In the complexes described here, the metal cation is surrounded by two triphenylene groups and 10 dodecyloxy chains. Therefore, the triphenylene ligand used most likely protects the metal cation preventing the decomposition of the complex. In fact, as discussed below, the anion has virtually no influence on the mesomorphic behavior of the system.

The free isocyanide ligand melts directly into the isotropic liquid and is consequently not a liquid crystal. However, all the gold and silver bis(isocyanide) complexes display enantiotropic mesomorphism in the temperature range 35–80 °C. It is not surprising that the melting and clearing points are almost identical for all these ionic compounds, as the promesogenic cation is similar, and the effect of the anion on the transition temperatures is insignificant.

The textures observed by POM on cooling from the isotropic liquid are similar for all compounds and show sandy-like textures (Fig. 3). Although these textures are not specific to a

Table 1 UV-Visible and luminescence data for the free isocyanide, and for the gold and silver complexes, in dichloromethane solution at 298 K (10^{-6} M)

Compd.	λ ($\varepsilon/10^3$)	λ_{ex}	λ_{em}	τ^a	Φ_{fl}
CNR	345 (4.4), 307 (33.0), 279 (149.4), 270 (97.4), 260 (73.7)	330	385	8.35	0.17
1	338 (8.8), 301 (51.1), 278 (243.6), 268 (161.1), 259 (124.7)	339	385	7.76	0.16
2	340 (5.7), 299 (49.2), 278 (220,1), 268 (146.7), 259 (114.9)	339	385	8.03	0.14
3	341 (15.2), 298 (54.6), 278 (199.3), 268 (142.6), 259 (107.2)	334	385	6.86	0.08
4	346 (12.4), 306 (72.4), 279 (272.9), 272 (192.6), 260 (142.4)	331	385	4.62	0.11

λ: nm. $\varepsilon/10^3$: M^{-1} cm^{-1}. [a] Lifetime in nm τ ($\pm$ 0.03).

Table 2 Optical, thermal, and thermodynamic data for the free isocyanide ligand and its silver and gold complexes **1–4**

Compound	Transition[a]	Temperature[b] (°C)	ΔH^b (kJ mol^{-1})
CNR	Cr → I	49	81.6
1	Cr → Col_{rec}	35[c]	55.9
	Col_{rec} → I	80[c]	2.3
2	Cr → Col_{rec}	39[c]	83.6
	Col_{rec} → I	78[c]	7.6
3	Cr → Col_{rec}	36[d]	72.3
	Col_{rec} → I	75	9.5
4	Cr → Col_{rec}	43[d]	88.3
	Col_{rec} → I	75	7.0

[a] Cr, crystal phase; Col_{rec}, rectangular columnar mesophase; I, isotropic liquid. [b] Data collected from the second heating DSC cycle. The transition temperatures are given as peak onsets. [c] Heating cycle at 20 °C min^{-1}. The rest of the data was taken at 10 °C min^{-1}. [d] Data collected from the first heating DSC cycle.

particular type of mesophase, they are compatible with columnar mesophases. This was confirmed by X-ray studies.

X-ray characterization

The X-ray experiments were conducted at several temperatures, on heating and on cooling from the isotropic liquid. In these systems, the emergence of a two-dimensional columnar mesophase characterized by a rectangular symmetry and expanded lattice parameters is observed. All the S/WAXS profiles of the mesophases are identical and show numerous sharp, small-angle reflections (Fig. 4 and Fig. S32), unambiguously indexed according to a centered rectangular lattice with plane group *c2mm* (Table S1). In addition, two broad and semi-diffuse signals in the wide-angle range signal, corresponding respectively to the orthogonal stacking of the triphenylenes correlated over short distances, h_π (*ca.* 3.5–3.6 Å), and to the liquid-like lateral distances between molten peripheral chains and spacer,

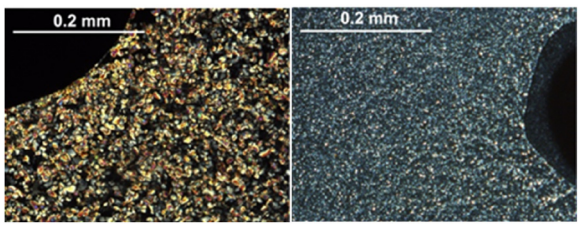

Fig. 3 Optical polarizing microscopy photographs (crossed polarizers) on cooling from the isotropic phase and after annealing of $[Ag(CNR)_2]BF_4$ (**2**) at 70 °C (left), and $[Au(CNR)_2]NO_3$ (**3**) at 60 °C (right).

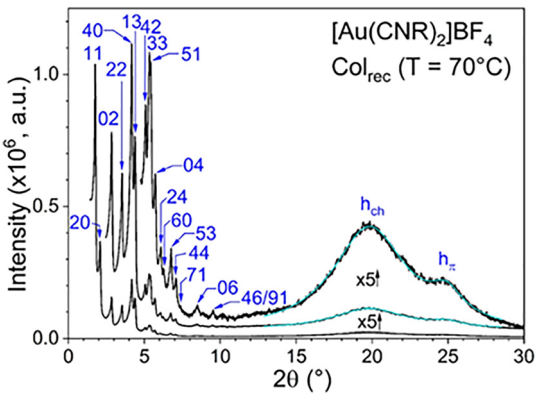

Fig. 4 S/WAXS pattern of $[Au(CNR)_2]BF_4$ (**4**), recorded at 70 °C, chosen as a representative example. S/WAXS patterns of the other compounds and the complete indexation table can be found in the SI (Table S1 and Fig. S32).

h_{ch} (*ca.* 4.4–4.6 Å), are observed systematically. The inhomogeneous intensity distribution of the higher order diffraction peaks reflects the presence of a complex, highly-ordered 2D structure, characterized by the effective segregation of the molecular constituents into alternating electron-rich and electron-deficient domains within the lattice, specifically, the triphenylene units, the metallic fragments, and the aliphatic continuum, respectively. The profiles are in full agreement with the double-block molecular structure of the complexes and reveal the characteristic features of multicolumnar mesophases *i.e.* mesophases containing several columns per lattice formed by the simultaneous stacking of triphenylene (TP) discs in one-dimensional columns on the one hand, and by the aggregation of metallic fragments $[M(CNPh)_2]$ assembled into filaments running parallel between the TP columns on the other, all separated by fused chains merged into an infinite continuum, as previously observed in related structures.[40,42,44] The structural characteristics of the mesophases are relatively independent of the metal or type of anion used, and of the temperatures at which the experiments were conducted.

Thus here too, the induction of mesomorphism is as expected to be predominantly governed by the triphenylene units, which preferentially assemble into one-dimensional columns and nanosegregate from both the peripheral alkyl chains and the metallic aggregates, which are confined into other distinct domains.

To further elucidate the supramolecular organization, we conducted comprehensive geometrical analysis as follows. The

Table 3 Geometrical and structural parameters of the mesophases obtained from S/WAXS

Compound	T^a (°C)	Phase[b]	2D lattice parameters[c]	Z^c	A	$V_{mol}{}^d$	ρ	$N_{mol}{}^e$	$h_{mol}{}^f$	$h_\pi{}^g$	$Z_{col,M(CNPh)2}{}^h$	$Z_{col,TP}$
1	70	Col_{rec}-*c2mm*	a = 88.54 b = 65.33 a/b = 1.35	Z = 2	5784.42	4910	0.98	4	3.39	3.59	2	8
2	70	Col_{rec}-*c2mm*	a = 89.02 b = 66.04 a/b = 1.34	Z = 2	5879.12	4921	0.99	4	3.35	3.52	2	8
3	60	Col_{rec}-*c2mm*	a = 87.74 b = 66.40 a/b = 1.32	Z = 2	5826.43	4870	1.02	4	3.34	3.53	2	8
4	70	Col_{rec}-*c2mm*	a = 84.84 b = 62.29 a/b = 1.36	Z = 2	5284.68	4900	1.02	4	3.71	3.57	2	8

[a] T: temperature of the measurement. [b] Col_{rec}: rectangular columnar mesophase. [c] a, b: lattice parameters (Å) and lattice parameter ratio, Z: number of motifs (repeated patterns) in the *c2mm* lattice, $A = a \times b$ lattice area (Å^2). [d] V_{mol}, ρ: calculated molecular volume (Å^3) and density (g cm^{-3}). [e] N_{mol}: number of the ionic metallic complex (formula) per lattice. [f] $h_{mol} = N_{mol} \times V_{mol}/A = \approx h_\pi$: molecular slice thickness along TP columns (Å), $n_{TP,mol}$ and $n_{M(CNPh)2/mol}$: number of TP units and metallic fragments per molecular unit (stoichiometry 2 : 1). [g] h_π: average π-stacking distance (Å). [h] $Z_{col,TP} = N_{mol} \times n_{TP/mol}$, number of TP-based columns per lattice; $Z_{col,M(NCPh)2} = N_{mol} \times n_{M(CNPh)2/mol}/2$, number of metallic fragments/anion columns per lattice (associated in pairs).

relationship between the volume of the formula unit (V_{mol}) and the full lattice area (A) is expressed by the equation:

$$N_{mol} \times V_{mol} = h_{mol} \times A \quad (1)$$

which establishes a quantitative correlation between N_{mol}, the number of formula units within the lattice, and h_{mol}, the thickness of the elementary lattice characteristic of the mesophase. For all the compounds, N_{mol} is found to be equal to 4, for h_{mol} values falling in the same range as h_π (see Table 3). The closeness between h_{mol} and h_π values suggests a nearly orthogonal stacking of the triphenylene discs within the columns. This geometrical analysis further reveals that the number of triphenylene cores per lattice is consistently equal to 8 (*i.e.* = $n_{TP,mol} \times N_{mol}$, each ionic complex bearing two triphenylene subunits each, $n_{TP,mol}$ = 2), indicating the presence of 8 triphenylene-based columns ($Z_{col,TP}$). The metallic fragments must adhere to the molecular constraints and the *c2mm* symmetry of the phase.

A plausible supramolecular organization for this multicolumnar mesophase can be described as follows: the metallic fragments, aggregated in pairs, due to lattice symmetry and molecular constraints, are localized at the nodes of the rectangular lattice (specifically at the corners and centre), thus giving a value of 2 such fragments in the lattice ($Z_{col,M(CNPh)2}$ = 2). These metallic pairs are interwoven within a sub-network of 8 triphenylene-based columns, with both components separated by an aliphatic continuum. This arrangement is fully consistent with the molecular structure of the complexes, the experimentally determined lattice dimensions, and the rectangular centred symmetry, as illustrated in Fig. 5. Such a highly ordered and interconnected structure with nanosegregated ionic domains is expected to enhance the material's ionic conductivity along the columnar axes, while the separation by the aliphatic continuum may contribute to improved thermal stability and controlled self-assembly behaviour. Finally, it should also be said that although the anions have not been localized in any compound, they must be located around the positively charged metal ion.[47,49]

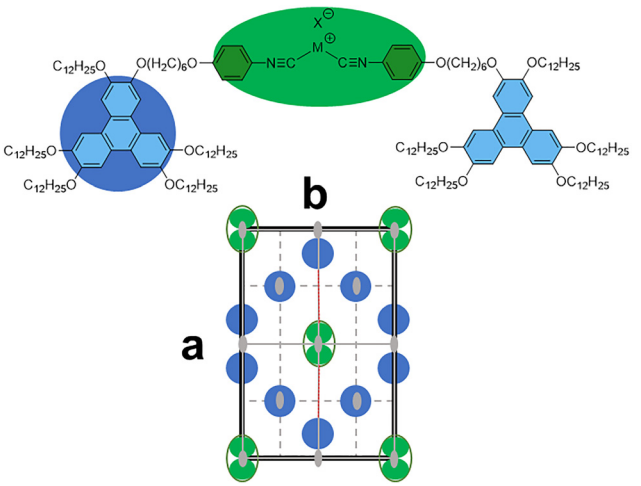

Fig. 5 Molecular structure and illustration of a possible 2D arrangement of the ionic complexes in the Col_{rec} mesophase (*c2mm* symmetry). The blue disks correspond to TP-based columns, and the green ovals correspond to paired metallic-based aggregates; the aliphatic chains, occupying the white areas, are not shown for clarity; lines and symbols in grey, symmetry elements (2-fold rotation axes, mirror lines and glide lines) of the planar group *c2mm*. The image represents the projection of the structure along the columnar axis and shows only the average symmetry of the stacking of triphenylene discs and organometallic fragments.

Impedance spectroscopy measurements

The formation of Col_{rec} mesophases in these metal complexes leads to nanosegregated ionic domains that, in combination with the fluid nature of the mesophase, could trigger the mobility of the NO_3^- and BF_4^- counterions along the one-dimensional columns. To study the dielectric behavior of these complexes, temperature-dependent impedance spectroscopy measurements were conducted in the solid, liquid crystal and isotrope phases.

In Fig. 6, impedance spectra from all compounds are shown on complex impedance plane plots of imaginary *vs.* the real part

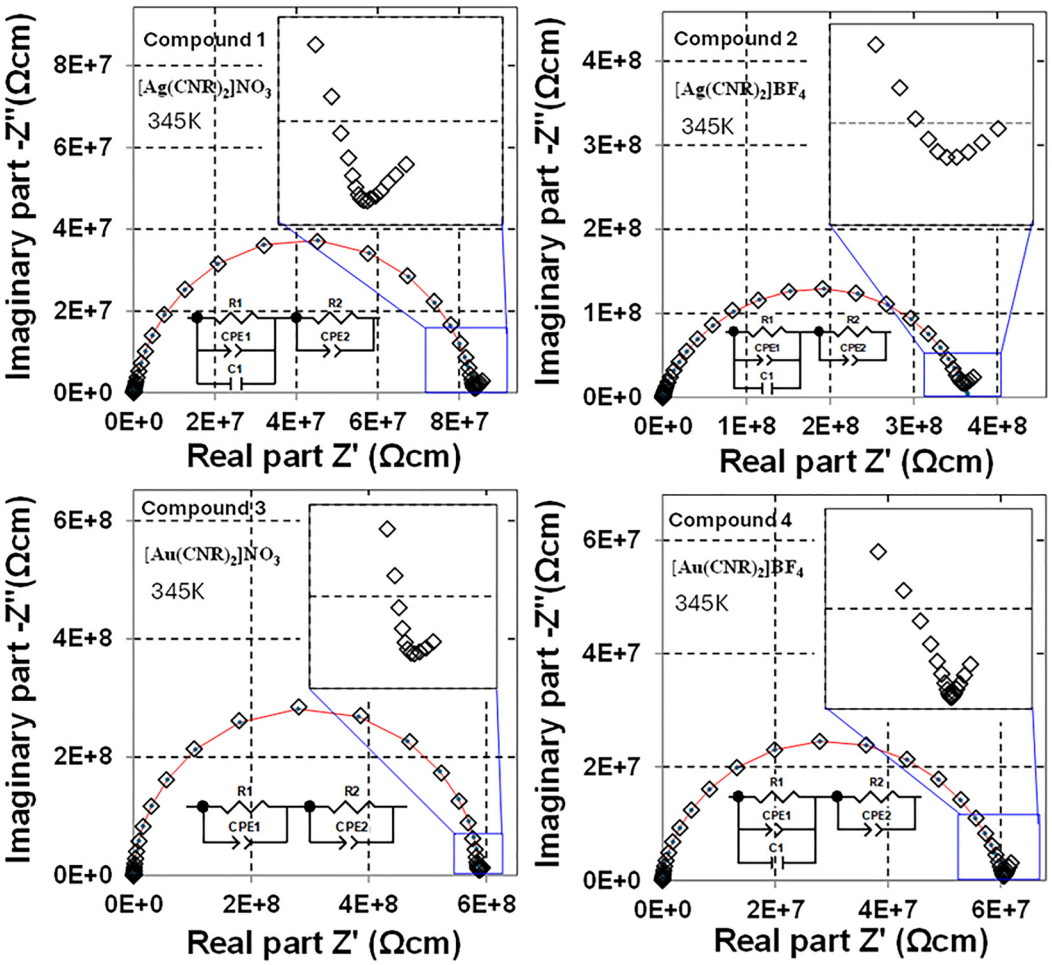

Fig. 6 Complex impedance plane plots of imaginary *vs.* the real part of the impedance Z'' *vs.* Z' at 345 K in the mesophase for all compounds **1–4**, expressed in specific units of resistivity ρ (W cm). Open diamond symbols correspond to the data, small blue dots and red lines represent equivalent circuit fits using the circuit models displayed below each semicircle.

of the impedance (Z'' *vs.* Z'), where the data were collected at 345 K upon heating in each instance. At 345 K, all compounds are still in the mesophase but close to the clearing temperature. Open diamond symbols correspond to the data, whereas the small blue dots and red lines represent the curves that had been fitted to the data using the respective equivalent circuits shown below each semicircle. Each figure panel displays one main semicircle, where all semicircles are suppressed below the *x*-axis to various degrees and show a certain degree of asymmetry. The suppression of the semicircle below the *x*-axis can be modelled by replacing or adding constant-phase elements to the standard parallel and ideal RC element (R1-CPE1-C1 or R1-CPE1), whereas the asymmetry is taken care of by adding an additional R2-CPE2 element. It should be noted that the diameter of the main semicircle corresponds to the sum of the resistors R1 + R2, and the two R-CPE-C and R-CPE elements may thus not be regarded as independent. However, it turned out from the fits that R2 is always rather small as compared to R1 and hardly contributes to the total resistivity ρ. It is interesting to note that the data from compound **3** display hardly any asymmetry but show signs of a very small overlapping semicircle at high frequency (not resolved here), which can be modelled with two series R1-CPE1 and R2-CPE2 elements.

It can further be noticed that the data from all compounds display the signs of an additional low frequency contribution (see blue boxes and blue lines) in the form of an approximately linear impedance pike. These pikes are displayed in the insets of each figure panel, showing the magnified low frequency data. These pikes are the hallmark features of ionic conductivity, which may well be associated with the mobility of the NO_3^- or BF_4^- anions in the columnar mesophases, *via* the nanochannels formed during the solid – mesophase phase transitions in each compound. Further clear indications for ionic conductivity can be found on plots of the real part of the capacitance C' *vs.* frequency (C' *vs.* f), where the capacitance C' massively and linearly increases at the low frequency with decreasing frequency. Examples for C' *vs.* f data sets can be found in the SI (Fig. S34).

Apparently, the ionic conductivity σ (= $1/\rho$) at 345 K (71.85 °C) in the mesophase was found to be best (lowest resistivity/smallest semicircle) for compound **4** $[Au(CNR)_2]BF_4$, *i.e.* σ (345 K) = 1.64×10^{-8} S cm^{-1} upon heating. For

comparison, in compound **1** $[Ag(CNR)_2]NO_3$, σ (345 K) = 1,18 × 10^{-8} S cm^{-1}, in compound **2** $[Ag(CNR)_2]BF_4$, σ (345 K) = 2,73 × 10^{-9} S cm^{-1}, and in compound **3** $[Au(CNR)_2]NO_3$, σ (345 K) = 1,70 × 10^{-9} S cm^{-1}, all upon heating. Note that conductivity increases by increasing the molecular slice thickness along TP columns (see Table 2) *i.e.* when the triphenylene discs are not so well associated within the columns that form the orthogonal π-stacking. In such a situation, anionic diffusion in the mesophase should be favoured, facilitating the mobility of ions through the continuous nanochannels of the Col_{rec} mesophase.

These conductivity values are similar to those reported for the nematic mesophase of ionic 8-diaza-crown ether liquid crystals, although ion conduction is based on the movement of K^+ and Li^+ charge carriers in this case.[50] Counterion mobility in crown ethers based on 12-crown-4 and 18-crown-6 fragments has been described in Col_{rec} mesophases, reaching conductivity values of the order of 10^{-7}–10^{-8} S cm^{-1} for I^-, and 10^{-8}–10^{-9} S cm^{-1} for SCN^- and BF_4^- counteranions.[51] Even in bicontinuous cubic mesophases of $LiBF_4$-doped ionic liquid crystals, which open three-dimensional continuous pathways, the counterion conductivity does not exceed values of 10^{-7} S cm^{-1}.[52] By contrast, large conductivities of the order of 10^{-3}–10^{-5} S cm^{-1} have been achieved by mixing ionic liquid crystals with ionic liquids, which improves the ion-conductive layers in the mesophase.[53] In this context, it is probable that the rather bulky nature of the NO_3^- and BF_4^- counterions here hinders higher anion mobility in the Col_{rec} mesophase of our metal complexes under anhydrous conditions.

Fitted parameters from equivalent circuit modelling

The fitted values for the resistors were added (R1 + R2) to represent the diameter of the main semicircles, which corresponds to the total ionic resistivity of each compound. The total resistivity was plotted *vs.* temperature (*T*) in Kelvin (K) for each compound as shown in Fig. 7 (compound **1** and **2**) and Fig. 8 (compound **3** and **4**) below. The data from the fits for heating and cooling are shown. In the upper panels, the data are plotted on semi-logarithmic axes of $\log_{10}$(resistivity) *vs.* *T*, whereas the lower panels display the data in the mesophase temperature range on Arrhenius axes of ln(resistivity) *vs.* 1/*T* (1/K) to determine the activation energies E_A.

It can be seen at the left panels of Fig. 7 that compound **1** shows unclear trends of resistivity *vs.* *T* upon heating within the mesophase, as compared to cooling where the curve can be linearized on Arrhenius axes (see the lower left panel). This fact suggests that the mesophase in compound **1** formed on heating from the crystalline solid is orientationally more disordered than that forming upon cooling from the isotropic liquid, generating non-continuous conduction pathways at temperatures near to the mesophase-isotropic liquid phase transition that causes notable changes in the resistivity curve. In fact, two different regimes with different activation energies (0.90 and 1.23 eV) can also be seen on cooling. This slight change in the activation energy near 345 K may again be associated with the rearrangement of the triphenylene metal–organic units upon cooling through the mesophase. The data upon heating in the

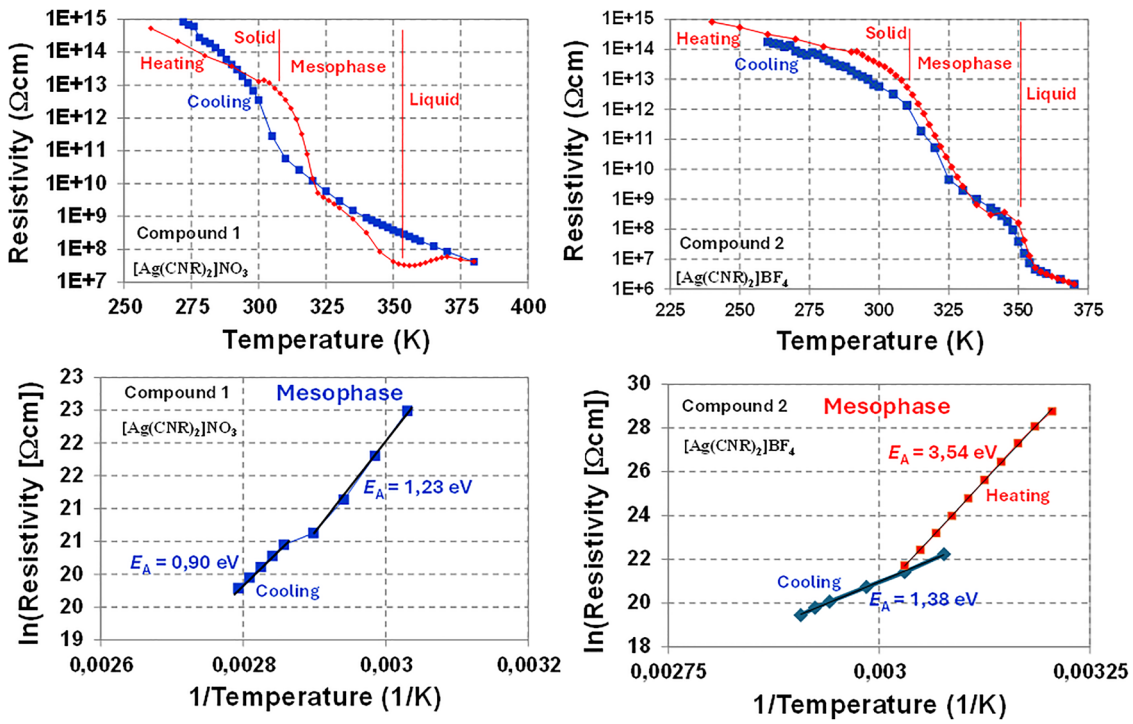

Fig. 7 Resistivity (Ω cm) *vs.* temperature (*T*) plots upon heating (red symbols and lines) and upon cooling (blue symbols and lines) for compounds **1** and **2**. In the lower panels, the data are plotted on Arrhenius axes for the temperature ranges only where the compound is in the mesophase.

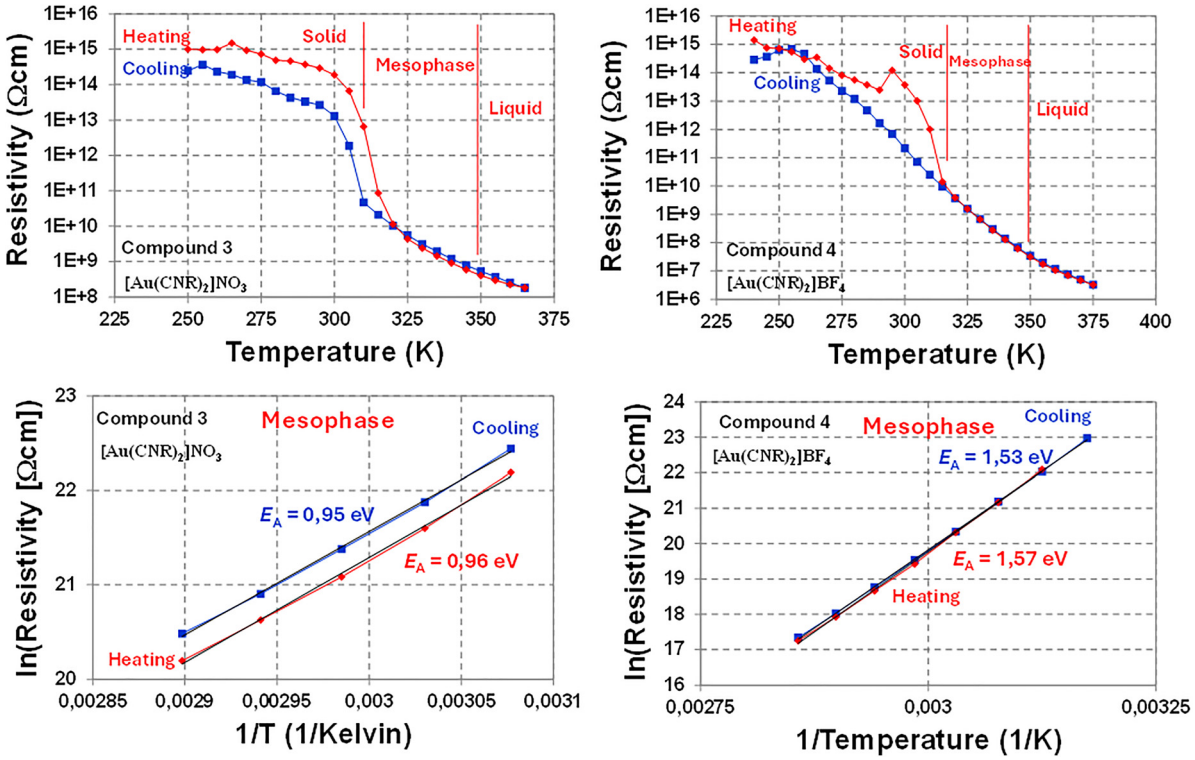

Fig. 8 Resistivity (Ω cm) *vs.* temperature (*T*) plots upon heating (red symbols and lines) and upon cooling (blue symbols and lines) for compounds **3** and **4**. In the lower panels, the data are plotted on Arrhenius axes for the temperature ranges only where the compound is in the mesophase.

mesophase could not be linearized adequately on Arrhenius axes and are thus not displayed.

The resistivity *vs.* *T* data for compound **2** are displayed in the right panels of Fig. 7. It can be seen that the reversibility is much better compared to compound **1**, since the heating and cooling curves are similar qualitatively and quantitatively. Within the mesophase, two clearly different regimes can be identified, where the resistivity drops quickly upon heating across the solid-mesophase transition. This may likely be related to the formation of the mesophase and the rearrangement of the triphenylene units. Therefore, the activation energy of 3.54 eV in this region should be considered with care, since it is unlikely to be related to thermally activated ionic charge transport, but with the phase transition. At higher temperatures within the mesophase formed on cooling, the activation energy (1.38 eV) is lower and in a similar range as for compound **1**, and may thus be more likely to represent the ionic charge transport activation energy, as compared to the high 3.54 eV value. In the lower temperature range within the mesophase, the data could be linearized adequately only upon heating, and *vice versa*, and therefore only the respective linear curves are displayed in the lower panel on Arrhenius axes.

The equivalent data for compounds **3** and **4** are displayed in Fig. 8. It can be seen that both compounds show good reversibility with a slight hysteresis in compound **3**, whereas compound **4** shows ideal reversibility for heating and cooling curves. The activation energies displayed are similar to each other for heating and cooling, confirming the excellent reversibility. Considering the generally lower resistivity in compound **4**, it may be considered most promising.

Conclusions

This study shows that the organic/inorganic nanosegregated multicolumnar mesophases based on the easily accessible bis(isocyanide) metal complexes of the type $[M(CNR)_2]Y$ (CNR = 2-(6-(4-isocyanophenoxy)hexyloxy)-3,6,7,10,11-pentakisdodecyloxytriphenylene; M = Ag, Au; Y = NO_3^-, BF_4^-) can provide well organized nanochannels with tunable ion transport properties. All the metal bis(isocyanide) complexes display thermotropic rectangular columnar mesophases, whose structure consists of the stacking of triphenylene disks into one-dimensional columns, and segregated peripheral alkyl chains and metallic aggregates, both of which are confined into other distinct columnar domains. This confinement of the inorganic fragments between triphenylene columns and fused chains is most likely the reason why the thermal behavior of the complexes is quite independent of the metal (Au or Ag) or type of anion (NO_3^- or BF_4^-) used. However, the nanosegregated ionic domains in the rectangular columnar mesophase create well-defined ion transport pathways for the NO_3^- and BF_4^- counterions, enabling conduction in these materials. Notably, the ionic conductivity in these mesophases increases regularly in the order **3** < **2** < **1** < **4**, from 1.70×10^{-9} to 1.64×10^{-8} S cm^{-1}, as the molecular slice thickness increases along the columns. Although conductivities of the order of

10^{-3} S cm^{-1} are required for commercial applications, the dielectric behavior described herein for these materials allows shedding light on the ion conduction mechanism that occurs in the mesophase of ionic metal complexes, of which there are few studies described in the literature. These findings demonstrate the key role of packing efficiency to modulate ion transport in soft materials, and the potential of organic/inorganic nanosegregated mesophases to develop advanced ion-conducting materials. In addition, the silver and gold complexes display fluorescence related to the triphenylene core in solution.

Author contributions

All of the authors have contributed equally to this paper.

Conflicts of interest

There are no conflicts to declare.

Data availability

The data supporting this article have been included as part of the supplementary information (SI). Supplementary information: materials and methods, full details of synthetic methods, spectroscopic and analytical data for the new compounds, MALDI-TOF mass spectra, DSC thermograms not included in the text, X-ray diffraction patterns not included in the text and capacitance data not included in the text. See DOI: https://doi.org/10.1039/d5tc03933a.

Acknowledgements

This work was sponsored by the University of Valladolid. C. C. and R. S. acknowledge the Community of Madrid and the UCM for the financial support under Grant no. PR17/24-31905 (Project: MetaBatt, Call: Línea A: Doctores emergentes). Action funded by the Community of Madrid through the Multiannual Agreement for the regulation of the cooperation framework within the Regional System of Scientific Research and Technological Innovation, signed between the Community of Madrid and the UCM, within the framework of the 6th PRICIT (Regional Plan for Scientific Research and Technological Innovation for the 2022–2025 period). R. S. acknowledges the AEI grants: PID2020-118078RB-I00 and PID2023-148884OB-I00. B. D. thanks the CNRS and the University of Strasbourg for constant support, and Dr B. Heinrich for the S/WAXS measurements.

Notes and references

1 K. Goossens, K. Lava, C. W. Bielawski and K. Binnemans, *Chem. Rev.*, 2016, **116**, 4643–4807.
2 S. Chen and S. Eichhorn, *Isr. J. Chem.*, 2012, **52**, 830–843.
3 S. K. Pal and S. Kumar, *Biosens. Nanotechnol.*, 2014, **9**, 267–314.
4 Q. Gao, C. Zou and W. Lu, *Chem. – Asian J.*, 2018, **13**, 3092–3105.
5 T. Kato, M. Yoshio, T. Ichikawa, B. Soberats, H. Ohno and M. Funahashi, *Nat. Rev. Mater.*, 2017, **2**, 17001.
6 N. Kapernaum, A. Lange, M. Ebert, M. A. Grunwald, C. Haege, S. Marino, A. Zens, A. Taubert, F. Giesselmann and S. Laschat, *ChemPlusChem*, 2022, **87**, e202100397.
7 M. Pastor, C. Cuerva, J. Campo, R. Schmidt, M. R. Torres and M. Cano, *Materials*, 2016, **9**, 360.
8 M. Marcos, A. Concellón, A. Terrel, R. I. Merino, R. M. Tejedor, J. Barberá, J. L. Serrano and S. Uriel, *J. Mater. Chem. C*, 2025, **13**, 14657–14664.
9 S. J. Devaki and R. Sasi, in *Prog. Dev. Ion. Liq.*, ed. S. Handy, InTech, 2017.
10 K. Binnemans, *Chem. Rev.*, 2005, **105**, 4148–4204.
11 M. Yoshio, T. Mukai, H. Ohno and T. Kato, *J. Am. Chem. Soc.*, 2004, **126**, 994–995.
12 B. Soberats, M. Yoshio, T. Ichikawa, X. Zeng, H. Ohno, G. Ungar and T. Kato, *J. Am. Chem. Soc.*, 2015, **137**, 13212–13215.
13 W. Dobbs, B. Heinrich, C. Bourgogne, B. Donnio, E. Terazzi, M. E. Bonnet, F. Stock, P. Erbacher, A. L. Bolcato-Bellemin and L. Douce, *J. Am. Chem. Soc.*, 2009, **131**, 13338–13346.
14 P. H. J. Kouwer and T. M. Swager, *J. Am. Chem. Soc.*, 2007, **129**, 14042–14052.
15 N. D. Suhan, S. J. Loeb and S. H. Eichhorn, *J. Am. Chem. Soc.*, 2013, **135**, 400–408.
16 L. Veltri, V. Maltese, F. Auriemma, C. Santillo, S. Cospito, M. La Deda, G. Chidichimo, B. Gabriele, C. De Rosa and A. Beneduci, *Cryst. Growth Des.*, 2016, **16**, 5646–5656.
17 K. Takagi, K. Yamauchi, S. Kubota, S. Nagano, M. Hara, T. Seki, K. Murakami, Y. Ooyama, J. Ohshita, M. Kondo and H. Masu, *RSC Adv.*, 2016, **6**, 9152–9159.
18 A. Alam, J. Motoyanagi, Y. Yamamoto, T. Fukushima, J. Kim, K. Kato, M. Takata, A. Saeki, S. Seki, S. Tagawa and T. Aida, *J. Am. Chem. Soc.*, 2009, **131**, 17722–17723.
19 J. J. Lee, A. Yamaguchi, M. A. Alam, Y. Yamamoto, T. Fukushima, K. Kato, M. Takata, N. Fujita and T. Aida, *Angew. Chem., Int. Ed.*, 2012, **51**, 8490–8494.
20 C. Cuerva, M. Cano and R. Schmidt, *Dalton Trans.*, 2023, **52**, 4684–4691.
21 C. Cuerva, J. A. Campo, M. Cano, R. Schmidt and C. Lodeiro, *J. Mater. Chem. C*, 2018, **6**, 9723–9733.
22 S. Kumar, *Chem. Soc. Rev.*, 2006, **35**, 83–109.
23 S. K. Pal, S. Setia, B. S. Avinash and S. Kumar, *Liq. Cryst.*, 2013, **40**, 1769–1816.
24 T. Wöhrle, I. Wurzbach, J. Kirres, A. Kostidou, N. Kapernaum, J. Litterscheidt, J. H. Haenle, P. Staffeld, A. Baro, F. Giesselmann and S. Laschat, *Chem. Rev.*, 2016, **116**, 1139–1241.
25 H. Goyal, P. Kumar and R. Gupta, *Chem. – Asian J.*, 2023, **18**, e202300355.
26 A. Schultz, S. Laschat, A. Saipa, F. Giesselmann, M. Nimtz, J. L. Schulte, A. Baro and B. Miehlich, *Adv. Funct. Mater.*, 2004, **14**, 163–168.
27 M. Kaller, C. Deck, A. Meister, G. Hause, A. Baro and S. Laschat, *Chem. – Eur. J.*, 2010, **16**, 6326–6337.
28 M. Kaller, S. Tussetschläger, P. Fischer, C. Deck, A. Baro, F. Giesselmann and S. Laschat, *Chem. – Eur. J.*, 2009, **15**, 9530–9542.

29 S. Laschat, A. Baro, T. Wöhrle and J. Kirres, *Liq. Cryst. Today*, 2016, **25**, 48–60.
30 J. Chen, Y. Sun, W. Zhao, J. Liu, J. Fang, T. Xu and D. Chen, *J. Mater. Chem. C*, 2021, **9**, 3871–3881.
31 H. Shimura, M. Yoshio, K. Hoshino, T. Mukai, H. Ohno and T. Kato, *J. Am. Chem. Soc.*, 2008, **130**, 1759–1765.
32 S. Kumar and S. K. Varshney, *Liq. Cryst.*, 2001, **28**, 161–163.
33 A. N. Cammidge and H. Gopee, *Chem. Commun.*, 2002, 966–967.
34 J. L. Schulte, S. Laschat, R. Schulte-Ladbeck, V. von Arnim, A. Schneider and H. Finkelmann, *J. Organomet. Chem.*, 1998, **552**, 171–176.
35 B. Mohr, G. Wegner and K. Ohta, *J. Chem. Soc., Chem. Commun.*, 1995, **10**, 995–996.
36 J. Shi, Y. Wang, M. Xiao, P. Zhong, Y. Liu, H. Tan, M. Zhu and W. Zhu, *Tetrahedron*, 2015, **71**, 463–469.
37 F. Yang, X. Bai, H. Guo and C. Li, *Tetrahedron Lett.*, 2013, **54**, 409–413.
38 R. Chico, C. Domínguez, B. Donnio, B. Heinrich, S. Coco and P. Espinet, *Cryst. Growth Des.*, 2016, **16**, 6984–6991.
39 V. Conejo-Rodríguez, B. Donnio, B. Heinrich, R. Termine, A. Golemme and P. Espinet, *J. Mater. Chem. C*, 2023, **11**, 1435–1447.
40 E. Tritto, R. Chico, G. Sanz-Enguita, C. L. Folcia, J. Ortega, S. Coco and P. Espinet, *Inorg. Chem.*, 2014, **53**, 3449–3455.
41 A. Miguel-Coello, M. Bardají, S. Coco, B. Donnio, B. Heinrich and P. Espinet, *Inorg. Chem.*, 2018, **57**, 4359–4369.
42 E. Tritto, R. Chico, J. Ortega, C. L. Folcia, J. Etxebarria, S. Coco and P. Espinet, *J. Mater. Chem. C*, 2015, **3**, 9385–9392.
43 R. Chico, E. de Domingo, C. Domínguez, B. Donnio, B. Heinrich, R. Termine, A. Golemme, S. Coco and P. Espinet, *Chem. Mater.*, 2017, **29**, 7587–7595.
44 E. de Domingo, C. Folcia, J. Ortega, J. Etxebarria, R. Termine, A. Golemme, S. Coco and P. Espinet, *Inorg. Chem.*, 2020, **59**, 10482–10491.
45 M. Barcenilla, M. J. Baena, B. Donnio, B. Heinrich, L. Gutiérrez, S. Coco and P. Espinet, *J. Mater. Chem. C*, 2022, **10**, 9222–9231.
46 E. de Domingo, G. García, C. L. Folcia, J. Ortega, J. Etxebarria and S. Coco, *Cryst. Growth Des.*, 2023, **23**, 6812–6821.
47 M. Benouazzane, S. Coco, P. Espinet, J. M. Martín-Alvarez and J. Barbera, *J. Mater. Chem.*, 2002, **12**, 691–696.
48 K. Jones, *Chemistry of The Nitrogen, in Comprehensive Inorganic Chemistry*, ed. J. C. BailarJr., H. J. Emeléus, R. Nyholm and A. F. Trotman-Dickenson, Pergamon Press, Oxford, 1973. vol. 2, p. 386.
49 J. T. J. Mathieson, A. G. Langdon, N. B. Milestone and B. K. Nicholson, *J. Chem. Soc., Dalton Trans.*, 1999, **2**, 201–208.
50 V. Conejo-Rodríguez, C. Cuerva, R. Schmidt, M. Bardají and P. Espinet, *J. Mater. Chem. C*, 2019, **7**, 663–672.
51 P. Staffeld, M. Kaller, P. Ehni, M. Ebert, S. Laschat and F. Giesselmann, *Crystals*, 2019, **9**, 74.
52 T. Ichikawa, Y. Sasaki, T. Kobayashi, H. Oshiro, A. Ono and H. Ohno, *Crystals*, 2019, **9**, 309.
53 J. Sakuda, M. Yoshio, T. Ichikawa, H. Ohno and T. Kato, *New J. Chem.*, 2015, **39**, 4471–4477.